Title

SHORT RANGE ORDER DIFFUSE INTENSITY CALCULATIONS IN THE CLUSTER VARIATION METHOD

Authors

Mohri, T.
Sanchez, J.M.
Fontaine, D. de

Publication Date

1984-12-01

Lawrence Berkeley Laboratory
UNIVERSITY OF CALIFORNIA

Materials & Molecular Research Division

Submitted to Acta Metallurgica

SHORT RANGE ORDER DIFFUSE INTENSITY CALCULATIONS IN THE CLUSTER VARIATION METHOD

T. Mohri, J.M. Sanchez, and D. de Fontaine

December 1984

Prepared for the U.S. Department of Energy under Contract DE-AC03-76SF00098

DISCLAIMER

LBL-18774

SHORT RANGE ORDER DIFFUSE INTENSITY CALCULATIONS IN THE CLUSTER VARIATION METHOD

T. Mohri, J.M. Sanchez*, and D. de Fontaine

Department of Materials Science
and Mineral Engineering,
University of California
and Lawrence Berkeley Laboratory
Berkeley, CA 94720

December 1984

*Columbia University, Henry Krumb School of Mines,
New York, New York 10027

Short Range Order Diffuse Intensity Calculations

in

the Cluster Variation Method

T. Mohri, J.M. Sanchez*, D. de Fontaine

University of California
Department of Materials Science and Mineral Engineering
Berkeley, CA. 94720

*Columbia University, Henry Krumb School of Mines, New York, N.Y. 10027

Abstract

The Cluster Variation Method (CVM) in the Tetrahedron-Octahedron approximation is used to calculate the short range order diffuse intensity distribution for binary ordered alloys. The results are compared to those derived by the Krivoglaz-Clapp-Moss (KCM) formula for various stoichiometric concentrations and temperatures. The CVM produces sharper diffuse intensity spectra than does the KCM formula, and better conserves the constancy of the integrated intensity. Use of the CVM further insures that the calculated short-range order intensity is consistent with derived phase diagrams and instability temperatures.

1. Introduction

The Cluster Variation Method (CVM) [1] has been used extensively to investigate phase equilibrium and phase diagram, for binary and multicomponent alloys. Only recently, however, has the method been used to study fluctuations [2] which, in alloys, give rise to the so-called short range order diffuse itensity. In this work we extend the calculations of reference [2], which were carried out for two dimensional systems, to the study of short range order diffuse intensity in fcc lattices.

We have recently completed the systematic investigation of fcc based "ordering phase diagrams" calculated by the Tetrahedron-Octahedron approximation of the CVM [3-7]. The clusters used in this approximation enabled both first and second neighbor pair interaction energies to be taken into account. It was thus possible to include in the phase diagrams all ordered superstructures of the fcc lattice derived by rigorous ground state analysis [8-11] for all possible values of the ratio α of second to first-neighbor interactions and for all possible concentrations $0 \leq c \leq 1$. Many important experimentally observed structures could thus be incorporated in the diagrams. For simplicity, the parameter α, the only physical one used in the calculations, was regarded as temperature and concentration-independent. The underlying fcc lattice was also regarded as rigid.

The resulting binary phase diagrams were called *prototype ordering phase diagrams* [3]. Seven such binary "prototype" phase diagrams were computed for the values of a α equal to -1.0, -0.2, 0.0, 0.25, 0.35, 0.45 and 0.55, conveniently grouped into three *ordering families*: $\langle 100 \rangle$ (corresponding to α = -1.0 and -0.2), $\langle 1\frac{1}{2}0 \rangle$ (α=0.25, 0.35, 0.45) and $\langle \frac{1}{2}\frac{1}{2}\frac{1}{2} \rangle$ (α=0.55), and also α=0.0, the latter being a degenerate case common to both $\langle 100 \rangle$ and $\langle 1\frac{1}{2}0 \rangle$ families. The "family" designation is based on the nature of the

special point ordering wave which first becomes unstable at the instability temperature, as explained in detail elsewhere [12].

The CVM-calculated diagrams, unlike those calculated by the Bragg-Williams (BW) method, are thought to be highly reliable, as attested by comparison with available Monte Carlo calculations [13-16]. Another important feature of the CVM, is that short-range order can be characterized quite readily, which is not possible by the BW method. In particular, pair and higher cluster probabilities can be calculated at all values of temperature and concentration in various ordered and disordered phase regions, thereby providing a local real-space representation of the state of order. More importantly, short-range order intensity (I_{SRO}), i.e. the Fourier transform of the pair correlation function, can be calculated, much as it is done in the Krivoglaz-Clapp-Moss (KCM) method, but in a way which is completely consistent with the derived phase diagrams [2]. Also, as shown elsewhere [2], the CVM-calculated I_{SRO} obeys the law of constancy of integrated I_{SRO} much more closely than that calculated by the KCM formula.

Hence, this paper, devoted primarily to short-range order, complements the previous one [3], henceforth designated as I, which was devoted to the equilibrium phase diagrams themselves. In Sect. 2, the general theory of I_{SRO} is recalled along with the relationship that exists between fluctuations and special-point (SP) instabilities. In Sec. 3, some examples of CVM I_{SRO} calculations are presented and compared with BW calculations. Some physical implications are then discussed in Sect. 4.

2. Theory

2.1 CVM Free Energy

Formally, the Free energy can be expressed as the minimum of the

following functional [17]:

$$F = \sum_J E(J)\ X(J) + k_B T \sum_J X(J)\ \ell n\ X(J) \qquad (1)$$

where E(J) and X(J) denote, respectively, the energy and the probability of the configuration J of the system (fora binary system with N lattice points, J takes 2^N values) and where k_B is the Boltzman constant and T the absolute temperature. The minimization of the functional F is carried out over all probability distributions X(J) subject to the constraint $\Sigma\ X(J)=1$. For large N, it is obviously impractical to carry out the summations explicitly. It is thus necessary to devise some approximate procedure for expressing the free energy.

The Cluster Variation Method (CVM), employed in I, provides an accurate approximation scheme for the calculation of the second term in Eq. (1), the configurational entropy S, which may be written as:

$$S = -k_B \sum_J X(J)\ \ell n X(J) \cong \sum_{n=1}^{n_0} \gamma_n\ S_n \qquad (2)$$

where the (positive or negative) γ_n integers are given by standard formulas [4,18], and depend on the geometry of the lattice and on the size of the largest cluster (n_0) included in the expansion. The partial entropy terms S_n are given by

$$S_n = -k_B \sum_{j=1}^{2^n} x_n(j)\ \ell n\ x_n(j), \qquad (3)$$

where $x_n(j)$ denotes the probability of occurrence of configuration j on the clusters of (n) lattice points, at equilibrium.

The cluster probabilities $x_n(j)$ are most conveniently described in terms of the multisite correlation functions ξ_n (4,18). Such correlation functions are defined as averages of products of the fundamental occupation number $\sigma(p)$ which, for binary systems, takes values +1or -1 if lattice point p is occupied by an A or a B atom, respectively.

$$x_{ns}(j) = \frac{1}{2^n}\left[1 + \sum_{n',s'} V_{nsn's'}(j)\,\xi_{n's'}\right] \tag{4}$$

where the subscript $s(s')$ is introduced to distinguish the shape of clusters of $n(n')$ lattice points. The matrix elements $V_{nsn's'}(j)$ are given by products of the $\sigma(p)$ and the sum runsover all subclusters $(n's')$ which are contained in a cluster (ns). An advantage of such a description of $x_{ns}(j)$ in terms of correlation variables is that the free energy is then expressed with independent variables only.

The average configurational energy, the first term on the right hand side of the Eq.(1), can also be described by a linear combination of multisite correlation functions [18,19]:

$$\langle E\rangle = \sum_J E(J)\,X(J) = E_0 + \sum_{n,s} \varepsilon_{ns}\,\xi_{ns} \tag{5}$$

where E_0 and ε_{ns} are, respectively, the energy of the completely disordered state and the n-body effective interaction energy:

$$E_0 = \frac{1}{2^N}\sum_J E(J) \tag{6}$$

and

$$\varepsilon_{ns} = \frac{1}{2^N}\sum_J V_{ns}(J)\,E(J). \tag{7}$$

In the present model, as mentioned in the Introduction, the energy approximation consists in effectively taking all energy coefficients ε_{ns} equal

to zero except those corresponding to first- and second-neighbor pairs. Thus the final expression for the energy is:

$$\langle E \rangle = \frac{1}{2} \varepsilon \sum_{p} \sum_{\rho_1} \langle \sigma(p)\, \sigma(p+\rho_1) \rangle + \frac{1}{2} \alpha\varepsilon \sum_{p} \sum_{\rho_2} \langle \sigma(p)\, \sigma(p+\rho_2) \rangle = \sum_{s=1}^{2} \varepsilon_{2,s} \xi_{2,s} \qquad (8)$$

where ε (positive) and $\alpha\varepsilon$ are, respectively, 1st and 2nd neighbor pair interaction energies, and ρ_1 and ρ_2 are, respectively, 1st and 2nd neighbor distances.

Substitution of Eqs.(2), (3) and (8) into Eq. (1) yields the final expression for the free energy f per lattice site:

$$f = \frac{F}{N} = \sum_{s=1}^{2} \varepsilon_{2,s} \xi_{2,s} + k_B T \sum_{n,s}^{n_0} \gamma_{ns} \sum_{j} x_{ns}(j) \ln x_{ns}(j) \qquad (9)$$

By means of Eqs. (4) and (5), the freeenergy is now expressed as a function of independent correlation variables (ξ_{ns}). This form of Eq. (9), however, assumes the equivalence of all lattice points, which is true only for disordered phases. In ordered phases, an additional parameter p is needed to distinguish non-equivalent sublattices, and, as a more general expression of Eq. (9), one can derive:

$$f = \frac{F}{N} = \frac{1}{L} \sum_{p=1}^{L} \left[\sum_{s} \varepsilon_{2,s} \xi_{2,s}(p) + k_B T \sum_{n,s}^{n_0} \gamma_{ns} \sum_{j} x_{ns}(j,p) \ln x_{ns}(j,p) \right] \qquad (10)$$

where the p summation is over the L sublattices.

In the present T-O CVM, the largest cluster (n_0) used are the Tetrahedron and Octahedron shown in Fig. 1. Ten correlation variables are deduced as independent variables for the disordered phase. The accuracy of the above CVM formulae have been demonstrated in extensive studies on phase diagram calculations [3-7]. More detailed derivations are found in the authors' previous papers [4-6,19].

2.2 Stability Analysis

Various thermodynamic properties can be derived from the free energy expressions, Eq. (9) (or 10). In particular, the main interest in this study is the response of the system to small deviations of the correlation variables from the equilibrium state. This is examined through the following free energy expansion in powers of the correlation variables around the equilibrium state [5,20].

$$F = F_0 + F_1 + F_2 + F_3 \ldots\ldots \tag{11}$$

where F_i is related to the i^{th} derivative of the free energy with respect to correlation variable(s) evaluated at the equilibrium state, F_0 being the equilibrium free energy. By assuming that the deviations are small enough to neglect terms of order higher than the third, Eq. (11) can be well approximated by

$$F \cong F_0 + F_2 \tag{12}$$

where F_1 vanishes at equilibrium.

The response of the system is therefore described by the 2nd order term, as expressed by the following quadratic form [5]:

$$\delta F = F - F_0 \cong F_2 = \frac{N}{2} \sum_{\ell\ell'} \sum_{pp'} f_{\ell\ell'}(p,p') \delta\xi_\ell(p)\, \delta\xi_{\ell'}(p') \tag{13}$$

where the indices ℓ and ℓ' refer to (n,s) and (n',s'), respectively, p and p' indicate the site dependence, and $f_{\ell\ell'}(p,p')$ is more explicitly given by

$$f_{\ell\ell'}(p,p') = \frac{\partial^2 f}{\partial\xi_\ell(p)\, \partial\xi_{\ell'}(p')} \tag{14}$$

If δF is positive for any virtual process induced by $\{\delta\xi\}$, the system remains at the original equilibrium state. This is expressed mathematically as the condition of positive definitness of the quadratic form (13). Conversely, as soon as δF becomes negative for some choice of $\{\delta\xi\}$ the system becomes

unstable and a transition to a more stable equilibrium state must occur.

Stability analysis is most conveniently carried out in k-space, the Fourier transformation of Eq. (13) yielding:

$$\delta F = \frac{N}{L} \sum_{h} \sum_{\ell\ell'} \Phi_{\ell\ell'}(k)\, \delta X_{\ell}(-k)\, \delta X_{\ell'}(k) \qquad (15)$$

with $\Phi_{\ell\ell'}(h)$ and $X_{\ell}(h)$ being the Fourier transforms, respectively, of $F_{\ell\ell'}(p,p')$ and $\xi_{\ell}(p)$.

The quadratic form in Eq. (15) can be written as a sum of squares:

$$\delta F = \frac{1}{2} \sum_{\ell} \sum_{k} \Delta_{\ell}(k)\, |\delta Z_{\ell}(k)|^2 \qquad (16)$$

in which $\Delta_{\ell}(h)$ are the eigenvalues of the matrix Φ and Z_{ℓ} are normal mode amplitudes.

The stability criterion is now restated mathematically in the following manner. If and only if all the eigenvalues are positive for all possible wave vectors k, stability prevails. Conversely, as soon as one of the eigenvalues goes through zero for some k_0, loss of stability occurs. The stability limit is, therefore, given by the vanishing of the determinant of the matrix $\Phi_{\ell\ell'}$:

$$|\Phi_{\ell\ell'}(k_0, T_0, C)| = 0 \qquad (17)$$

The highest temperature T_0 at which the above condition is satisfied is defined as the instability temperature and the particular wave vector k_0 for which it occurs is called the ordering wave.

A clear distinction must be made between the equilibrium order-disorder transition temperature T_t and the instability temperature T_0 [20]. The former is given by the existence of a common tangent between the free energy of the ordered and the disordered phases. The latter (T_0) is the one at which the metastable disordered phase becomes unstable, so that, below T_0, a concentration wave of wave vector k_0 will spontaneously increase in amplitude.

This process has been termed "spinodal ordering" [12]. At a second-order transition, the temperatures T_t and T_o coincide. Otherwise, at a first-order transition, the distance between T_t and T_o can be taken as a measure of the "strength" of the order of the transition. In I, the loci of some instability temperatures have been plotted as dotted lines on the calculated phase diagrams.

2.3 Short Range Order Diffuse Intensity

Although the formal theory of fluctuations is well known [21], its application to CVM derived free energies is very recent [2]. The study of fluctuations in alloys is most commonly carried out by using the theory of Krivoglaz [22] and Clapp and Moss [23] who derived an expression for the short range order diffuse intensity based on the Bragg-Williams approximation [24]. As shown elsewhere [2], however, marked improvement in the calculated short range order diffuse intensities follows from the use of the more accurate CVM free energies. The improvement in the caculated intensities is very significant since it is now possible to perform experimental intensity measurements very accurately.

The determination of the short range order diffuse intensity, I_{SRO}, requires the calculation of the pair correlation functions $\xi_2(r) = \langle \sigma(p)\ \sigma(p)+n \rangle$ for all distances r or, equivalently, the Fourier transform of such correlations. In the notation adopted here and also used in Ref. [2], the short range order intensity is written as:

$$I_{SRO} = \langle |\sigma(k)|^2 \rangle - |\langle \sigma(k) \rangle|^2 \qquad (18)$$

where $\langle \sigma(k) \rangle$ and $\langle |\sigma(k)|^2 \rangle$ are respectively, the Fourier transforms of the point $\langle \sigma(p) \rangle$ and pair $\langle \sigma(p)\ \sigma(p') \rangle$ correlation functions.

In order to calculate I_{SRO} or, more generally, the fluctuation spectrum of

the alloy, the usual approach is to study the system's response to an external inhomogeneous field. In the present case of a binary alloy, the inhomogeneous field is an effective chemical potential μ_p. As shown elsewhere [2], the multisite correlation functions are given by:

$$\langle \sigma_{p_1} \sigma_{p_2} \ldots\ldots \sigma_{p_n} \rangle = (-k_B T)^n \frac{1}{Z} \frac{\partial^n Z}{\partial \mu_{p_1} \partial \mu_{p_2} \ldots \partial \mu_{p_n}} \tag{19}$$

where μ_p is the inhomogeneous chemical potential field and Z is the partition function. In particular, for the pair correlations, Eq.(19) gives:

$$\langle \sigma_p \sigma_{p'} \rangle - \langle \sigma_p \rangle \langle \sigma_{p'} \rangle = -k_B T \frac{\partial^2 F}{\partial \mu_p \partial \mu_{p'}} \tag{20}$$

The Fourier transform of the right hand side of Eq. (20) can be performed by utilizing the translational symmetry of the disordered state so that one has, finally, the concise expression:

$$I_{SRO} = \langle |\sigma(k)|^2 \rangle - |\langle \sigma(k) \rangle|^2 = N k_B T \, \Phi^{-1}_{11}(k) \tag{21}$$

In this equation, Φ^{-1}_{11} is the first element of the matrix inverse to $\Phi(k)$, the Fourier transform of the matrix of the quadratic form (15)[2]. It is important to note that Eq. (21) is exact, in its general form. The result of its application will only be as accurate as the second-derivative matrix Φ, however, hence as accurate as the free energy F itself.

2.4 Ordering Wave

As mentioned above, and explained in detail elsewhere [12,24], fcc-based ordering systems can be generally classified according to four special-point (SP) families: $\langle 000 \rangle$, $\langle 100 \rangle$, $\langle 1\,{}^1/_2 0 \rangle$, $\langle {}^1/_2\,{}^1/_2\,{}^1/_2 \rangle$. It also follows that I_{SRO}

attains its maximum value at the wave vector k_0 whose Miller indices (in reciprocal space) are precisely the ones which define the ordering family in question.

If only first and second neighbor pair interactions are dominant, the family to which an ordering system belongs will depend uniquely on the ratio α. It is then convenient to represent the ordering families on a circular diagram [24], inspired by that first given by Clapp and Moss [25]. Such a diagram is shown here in Fig. 2 where V_1 and V_2 represent the first and second neighbor pair interactions, respectively. On the same figure are plotted calculated values of the reciprocal of the ratio of the short-range order intensity divided by the absolute temperature T/I, as a function of T, for various SP ordering waves, and for a values of α equal to -0.2, 0.35 and 0.55, at c=1/2.

In the Bragg-William (BW) approximation, leading to the Krivoglaz-Clapp-Moss (KCM) I_{SRO} formula, plots of T/I vs. T would be straight lines [26]. Here, however, the more accurate T-O CVM approximation has been used for the free energy. The resulting CVM I_{SRO} can formally be brought into the KCM form

$$I \propto [1 + 2c(1-c)\ V(k)/k_BT]^{-1}$$

but now, the k-space function V(k) must be expressed by means of effective pair interactions which depend on temperature [2]. It is this temperature-dependence which causes the curves in Fig. 2 to depart from straight-line behavior.

In agreement with theoretical expectations, I_{SRO} diverges at the instability temperature $k_0 = \langle 100 \rangle$ for $\alpha = -0.2$ (dotted line), at $k_0 = \langle 1\,{}^1/_2 0 \rangle$ for $\alpha = 0.35$ (full line), and at $k_0 = \langle {}^1/_2\,{}^1/_2\,{}^1/_2 \rangle$ for $\alpha = 0.55$. Much more information, suitable for comparison with experimental I_{SRO}, can be obtained by calculating the SRO diffuse intensity, not merely at the SP, but in, say a

planar section in k-space, as illustrated on some examples in the next section.

3. Computed SRO Intensity

As mentioned above, ordering phase diagrams were calculated previously, [3-7] for seven α values (-1.0, -0.2, 0.0, 0.25, 0.35, 0.45 and 0.55), covering all special point families. In this study, however, a typical α value is selected from each family (α=-0.20 for the $\langle 100 \rangle$ family, α=0.35 for the $\langle 1\,{}^1/_2\,0 \rangle$ family and α=0.55 for the $\langle {}^1/_2\,{}^1/_2\,{}^1/_2 \rangle$ family), and I_{SRO} calculations are carried out at the stoichiometric compositions of several stable ordered phases of each family.

3.1 $\langle 1\,{}^1/_2\,0 \rangle$ Family: α = 0.35

The phase diagram for α=0.35 obtained by T-O CVM is shown in Fig. 5 of Ref[3], the $\langle 1\,{}^1/_2 0 \rangle$ instability locus being given by the broken line in the diagram. One of the conspicuous features of this diagram is the change of the order of the transition with concentration: at c=0.5, the A_2B_2 phase is produced by a strongly 1st order transition, becoming second-order at the indicated tricritical point. The congruent transition to the A_2B and A_5B compounds is also 1st order, while the transition from the disordered to the A_3B ordered phase is mostly 2nd order. We shall focus here on concentrations c=0.50 and 0.33.

In each case, I_{SRO} maps are calculated at three temperatures, one at a high temperature of $T = 2T_O$, one just above the 1st order transition temperature T_t, and one just above the instability temperature T_O. Intensity contours are plotted, in a (100) reciprocal lattice plane, at the higher temperature in Fig. 3, and close to the instability ($T = T_O/0.95$) in Fig. 4.

Both CVM (left figure) and BW (right figure) calculations are reported. As expected, diffuse intensity maxima appear at the $1^1/_2 0$ points (and equivalent), with minima at the Bragg peak positions. The intensity distributions calculated by the CVM are seen to be sharper that those calculated by the BW formula. This is particularly apparent at the lower temperature, for reasons to be discussed presently.

In Fig. 5, CVM-calculated I_{SRO} plots are shown at $T = T_t/0.95$ for the two stoichiometries $c=^1/_3$ and $^1/_2$. What appears to be a concentration dependence of the intensity contours is, in fact, a temperature dependence: on a reduced scale of T/T_0 (the only pertinent one as far as I_{SRO} is concerned), the equilibrium transition temperature T_t is a relatively higher temperature at $c=^1/_2$ than is its counterpart at $c=^1/_3$. Hence, the intensity distribution at $T=T_t/0.95$ must peak more sharply at $1^1/_2 0$ for $c=^1/_3$ than it does for $c=^1/_2$. The concentration dependence of the contours at the same homologous temperature ($T = T_0/0.95$), for these two concentrations, is indeed small, as shown in Fig. 6.

The tendency for diffuse intensity peaks to become sharper as the instability (<u>not</u> the 1st order transition) temperature is approached is of course well-known, as can be qualitatively deduced from BW-related formulas. What is novel, is the increased sharpness of the CVM-calculated contours compared to the BW ones. The reason for that is that the CVM does much better at respecting the constancy of integrated intensity because the free energy calculated by the CVM is more accurate than that calculated by the BW approximation [2]. In the Krivoglaz-Clapp-Moss approximation (BW), the diffuse intensity tends to build up rather uniformly as the temperature is lowered towards T_0, and the integrated intensity increases correspondingly. In the CVM approximation, the integrated intensity remains more nearly

constant as T_0 is approached, so that, if intensity builds up at the special points, it must decrease relatively elsewhere, thus yielding sharper contours. The question of integrated intensity will be discussed further in Sec. 5.

3.2 ⟨100⟩ Family: $\epsilon = -0.20$

The relevant phase diagram, calculated previously, is shown in Fig. 8 of Ref.[3]. The ⟨100⟩ instability locus (ordering spinodal) is not shown, but T_0 at the stoichiometric compositions of $c=1/2$ and $1/4$ have been estimated, and I_{SRO} contour plots in (100) reciprocal lattice sections, at $T=T_0/0.95$, have been calculated for these two concentrations, as shown in Fig. 7. The corresponding BW contours are shown at the upper portion of the figure, for comparison. As expected, diffuse intensity maxima occur at the 100 positions (and equivalent). Again, the CVM contours are sharper than the BW contours, and the concentration dependence (at homologous temperatures), in the CVM I_{SRO} is very weak.

3.3 ⟨1/2 1/2 1/2⟩ Family: $\epsilon = 0.55$

The relevant phase diagram, calculated previously, is shown in Fig. 7 of Ref.[3], where the dotted line indicates the partially completed ⟨1/2 1/2 1/2⟩ instability locus (difficulties encountered with numerical convergence prevented its extension to lower concentrations).

Since diffuse intensity must peak at special points 1/2 1/2 1/2 (and equivalent), intensity contours are plotted in a (110) section in reciprocal space. Figure 8 shows such contours at $T=T_0/0.95$ and $c=1/2$. BW and CVM results are seen to differ significantly: the sharpness of the I_{SRO} distribution around the 1/2 1/2 1/2 maxima is more pronounced in the CVM calculation, and the contours have unexpected shapes. It was shown elsewhere

[12] that intensity contours in the vicinity of the relevant special point must resemble ellipsoids. Around $^1/_2{}^1/_2{}^1/_2$ maxima, all ellipsoids must have rotational symmetry about the [111] direction. This is borne out in the BW calculation, but the CVM-calculated contours exhibit an anomalous inner structure. More calculations will be needed to clarify this situation.

4. Real Space SRO

Although it is possible to calculate SRO Intensity from a BW Model, the BW free energy, by itself, contains no information about short-range correlations. By contrast, minimization of the CVM free energy functional returns values of pair, triangle, ..., multiplet correlation functions, up to the size of the largest cluster used in the configurational entropy expansion. Clapp pointed out [27] that knowledge of multisite correlations, or cluster concentrations, is essential if one wishes to picture the local atomic arrangements which characterize short-range order. That author was able to determine these correlations by maximizing the configurational entropy under the constraint of given pair probabilities, the latter obtained by Fourier inversion of experimentally measured I_{SRO}. Clapp used an approximate entropy expression, but it would have been possible to use the more accurate CVM formulas.

In the present instance, of known or assumed pair interaction parameters, the multisite probabilities are obtained directly from the minimized TO-CVM free energy as a by product. Point, pair, triangle,...., tetrahedron and octahedron cluster concentrations can be calculated from the ξ multiplet correlations according to Eq. (4). Results for the tetrahedra and octahedra concentrations are plotted in Fig. 9 as a function of reduced temperature for the case of $\alpha = 0.0$, $c = {}^1/_2$. The reciprocal I_{SRO}, multiplied by T, is also

plotted on another vertical scale, with same horizontal axis. As explained in connection with Fig. 2, the quantities T/Igoes to zero at T_o, meaning that the SRO intensity diverges at the instability. Cluster concentrations themselves do not behave anomalously at T_o, indeed, their values merely increase or decrease moderately from their complete-disorder values (at high temperature), as T_o is approached. No discontinuityis observed at the transition T_t. Those clusters which have same average (local) concentration as the whole system (here, $c=^1/_2$) have highest expectation values, or concentration, as expected: the two-A/two-B tetrahedron, the three-A/three-B octahedron. Both of these concentrations increase as the tendency for long-range AB ordering increases. All other cluster probabilities decrease as T_o is approached except that of the octahedron with two B (two A) atoms at opposite octahedral vertices. This is expected, as such octahedral configurations are those found in the ordered $L1_0$ structure (CuAuI). Conversely, the octahedra with same local concentration, but with B(A) atoms in nearest neighbor positions, are not enhanced since such concentrations are not found in the fully ordered LRO state. Thus, it is seen that the CVM distinguishes clearly between clusters of same average concentrations but different configurations.

The T/I curve of Fig. 9 shows the slight deviation from straight-line behavior already noted in Fig. 2. A deviation from linearity was observed experimentally by Bardhan, Chen and Cohen [30] in Cu_3Au crystals at the 100 and 300 superlattice positions, leading these authors to suspect the existence of "heterophase fluctuations," characterized by small metastable Cu_3Au embryos having relatively long lifetimes. Our calculations cannot confirm or deny the existence of heterophase fluctuations since such an analysis requires a non-infinitesimal stability study, which is beyond the scope of this work. Nevertheless, it is clear from our results that heterophase fluctuations are

not needed, in general, to account for non-linearities in the inverse intensity plot.

5. Integrated Intensity

It is well known that I_{SRO} integrated over the Brillouin zone must be proportional to the product $c_A c_B$ [or c(1-c)] of the average concentrations. The integrated intensity I_0 must therefore be temperature independent. In the Krivoglaz formulation, it is quite clear that I_0 increases as T decreases, becoming unbounded at T_0 [22]. Clapp and Moss [23] attempted to remedy this deficiency by normalizing I_{SRO} by a parameter proportional to the reciprocal of I_0 itself.

As shown elsewhere [2], the CVM I_{SRO} obeys the conservation of I_0 (unnormalized) far better than that derived from the BW approximation. This property is illustrated in Fig. 10 for the case $\alpha = 0.35$, $c = {}^1/_2$. At very high temperatures (~20 T_0), both BW (curve A) and CVM (curve B) the integrated intensity attains a constant value, which, in the units used here, is equal to unity. With decreasing temperature, however, the BW curve begins to deviate strongly from unity, while the CVM curve continues to hug the I_0=1 axis until very close to T_0. If a better CVM approximation had been used (larger clusters), the I_0 constancy rule would have been respected even more closely. It is indeed important to note that,as pointed out earlier [2], the failure of the integrated intensity rule is due to the inaccuracy of the free energy itself, not to the method by which the I_{SRO} is derived from it.

To save computer time, the curves of Fig. 10 were evaluated by using an approximate Brillouin zone integration technique: representative points were taken inside the first BZ, with step 0.1 along the cube axes, appropriate weights being assigned to each point taken, according to a method devised

originally for summing charge density [29,30].

6. Conclusion

At first sight, the differences between KCM-calculated and CVM-calculated I_{SRO} contours may not appear sufficiently dramatic to warrant the greater computational difficulty which the CVM entails. The authors believe, however, that in order to analyze diffuse intensity measurements (x-ray, neutron, electron diffraction), the CVM should be used exclusively in place of the older KCM formulation. The main reasons for advocating the switch are as follows: BW I_{SRO} contours may appear qualitatively acceptable, and may yield, by fitting, reasonable values of the pair interactions ε, but the phase boundaries derived from these fitted parameters by the BW free energy are expected to be highly unrealistic in most cases. It is therefore quite unsatisfactory to use an approximation for diffuse intensity calculations which is known to yield incorrect phase diagrams. The CVM-based formulation has no such deficiency since it gives accurate and mutually consistent values of I_{SRO}, phase boundaries, and transition (T_t) and instability (T_o) temperatures. This is an important point, as I_{SRO} measurements are the preferred ones for estimating the ε interaction parameters, and these, in turn, determine the thermodynamics of the solid solution and ultimately the phase diagram.

It has also been shown that the integrated intensity conservation rule is obeyed much more closely in the CVM-calculated I_{SRO}. This too is important, expecially when it is recalled that the reliability of experimental diffuse intensity measurements is often judged by how closely the zeroth Warren-Cowley parameter α_o approaches unity, which is equivalent to the requirement for I_{SRO} to sum to a constant inside the first Brillouin zone (or reciprocal unit

cell).

As explained above, the I_0 conservation results in a sharpening of diffuse intensity maxima as the instability temperature is approached. This property is further illustrated in Figs. 11 and 12 which are simulated I_{SRO} diffraction patterns, i.e. half-tone versions of the contour plots shown earlier. Both patterns are calculated for the case $\alpha = 0.35$, $c = {}^1/_2$, $T = T_0/0.95$, Fig. 11 according to the BW approximation, Fig. 12 according to the CVM. The CVM diffraction spots are much sharper and resemble closely those of electron diffraction patterns taken from Ni_3Mo alloys [31], for example.

Finally, it is now possible to produce very realistic CVM-generated phase diagrams of real alloy systems which, in itself, requires very precise values of interaction parameters [32-34]. Thus, comparison of theoretical and experimental I_{SRO} is expected to become increasingly important in the future.

ACKNOWLEDGEMENT

This work was initially supported by the Army Research Office (Durham), and partially supported by the Director, Office of Energy Research, Office of Basic Energy Sciences, Materials Sciences Division of the U. S. Department of Energy under Contract No. DE-AC03-76SF00098, LBL No. 18774.

REFERENCES

1. R. Kikuchi, Phys. Rev. **81**, 998 (1951).
2. J. M. Sanchez, Physica **111A**, 200 (1982).
3. T. Mohri, J. M. Sanchez and D. de Fontaine, Acta Metall. to be published
4. J. M. Sanchez and D. de Fontaine, Phys. Rev. **B 17**, 2926 (1978)
5. J. M. Sanchez and D. de Fontaine, Phys. Rev. **B 21**, 216 (1980).
6. J. M. Sanchez and D. de Fontaine, Phys. Rev. **B 25**, 1759 (1982).
7. J. M. Sanchez, D. de Fontaine and W. Teitler, Phys. Rev. **B 16**, 1465 (1982).
8. M. J. Richard and J. W. Cahn, Acta Metall. **19**, 1263 (1972).
9. S. M. Allen and J. W. Cahn, Acta Metall. **20**, 423 (1972).
10. M. Kaburagi and J. Kanamori, Progr. Theor. Phys. **54**, 30 (1979).
11. J. Kanamori and Y. Kakehashi, J. Phys. (Paris) **38**), C7-274 (1977).
12. D. de Fontaine, Acta Metall. **23**, 553 (1975).
13. R. A. Bond and D. K. Ross, J. Phys. F **12**, 597 (1982).
14. M. K. Phani, J. L. Lebowitz and M. H. Kalos, Phys. Rev. **B 21**, 4027 (1980).
15. K. Binder, J. L. Lebowitz, 13. M. K. Phani and M. H. Kalos, Acta Metall. **29**, 1655 (1981).
16. K. Binder, W. Kinzel and W. Selke, J. Magn. and Magn. Mat. **31-34**, 1445 (1983).
17. T. Morita, J. Phys. Soc. Japan **12**, 753 (1957); J. Math. Phys. 13, 115 (1972).
18. J. M. Sanchez, F. Ducastelle and D. Gratias, Physica A, (in press).
19. D. de Fontaine, in *Modualated Structure Materials*, NATO ASI Series E: No. 83, T. Tsakalakos, Editor, pp. 43-80, Martinus Nijhoff, Publ., Dondrecht (1984).
20. D. de Fontaine, Metall. Trans. A Vol. 12A, 559 (1981).

21. See for example, L. D. Landau and E. M. Lifshitz, Statistical Physics, Addison-Wesley, Reading, Massachussetts (1958).

22. M. A. Krivoglaz, Theory of X-ray and Thermal Neutron Scattering by Real Crystals, Plenum, New York, 1969.

23. P. C. Clapp and S. C. Moss, Phys. Rev. **142**, 418 (1966).

24. D. de Fontaine, Solid State Physics **34** (1979).

25. P.C. Clapp and S.C. Moss, Phys. Rev. **171**, 754 (1968).

26. P. Bardhan and J. B. Cohen, Acta Crys. **A 32**, 597 (1976).

27. P. C. Clapp, J. Phys. Chem. Solids **30**, 2589 (1969).

28. P. Bardhan, H. Chen and J. B. Cohen, Phils. Mag. [8] **35**, 1653 (1977).

29. D. J. Stukel, R. N. Euwema and T. C. Collins, Phys. Rev. **179**, 740 (1970).

30. D. J. Stukel and R. N. Euwema, Phys. Rev. **B 1**, 1635 (1970).

31. P. L. Martin, Ph.D. Dissertation, Dept. of Metall. Eng. and Mat. Science, Carnegie-Mellon University, Pittsburgh, PA (1982).

32. C. Sigli and J. M. Sanchez, Calphad **8**, 221 (1984).

33. J. M Sanchez, J. R. Barefoot, R. N. Jarrett and J. K. Tien, Acta Metall. **32**, 15 (1984).

34. C. Sigli and J. M. Sanchez, Acta Metall. (in press).

FIBURE CAPTIONS

Fig. 1 Basic clusters used in the Tetrahedron-Octahedron approximation.

Fig. 2 T/I - T diagram at c=0.50 for α = -0.2, 0.35 and 0.55. Dotted line, broken line, and full line represent $\langle 100 \rangle$, $\langle 1\frac{1}{2}0 \rangle$, and $\langle \frac{1}{2}\frac{1}{2}\frac{1}{2} \rangle$ ordering waves, respectively. The circle, right side above, shows special point families [25]. V_1 and V_2 are, respectively, 1st and 2nd neighbor pair interaction energies and $\alpha = V_2/V_1$.

Fig. 3 Equal intensity contours in a (001) reciprocal lattice plane calculated for α=0.35 at c=0.50 and $T=T_0/0.5$, where T_0 is the instability temperature. The left diagram is obtained by the present T-0 CVM calculation and the right diagram is calculated by BW based Krivoglaz-Clapp-Moss formula.

Fig. 4 Equal intensity contours in a (001) reciprocal lattice plane calculated for α=0.35 at c=0.50, $T=T_0/0.95$. The left figure is based on the CVM and the right one is based on the BW formula.

Fig. 5 CVM-calculated equal intensity contours in a (001) reciprocal lattice plane for α=0.35 at $T=T_t/0.95$, where T_t is the transition temperature. The left diagram is for c=1/3 and the right one is for c=0.5.

Fig. 6 CVM-calculated equal intensity contours in a (001) reciprocal lattice plane for α=0.35 at $T=T_0/0.95$. Theleft diagram is for c=1/3 and the right one is for c=0.5.

Fig. 7 Equal intensity-contour diagrams in a (100) reciprocal lattice plane calculated for α=-0.20 at $T=T_0/0.95$. The upper figure is based on the BW approximation and the two figures below arebased on the T-0 CVM. The left one is for c=0.25 and the right one is for c=0.5.

Fig. 8 Equal intensity contours in a $(1\bar{1}0)$ reciprocal lattice plane calculated for α=0.55 at $T=T_0/0.95$. The upper figure is based on the CVM and the one below is based on the BW approximation.

Fig. 9 Temperature dependence of cluster concentrations for α=0.35, c=0.50. Full lines and dotted lines represent octahedron and tetrahedron cluster concentrations, respectively. The T/I-T relationship is superimposed on the figure. The scale of T/I is found on the right vertical axis of the figure.

Fig. 10 Comparison of temperature dependence of integrated intensities for α=0.35 and c=0.50 over the 1st Brillouin zone. The horizontal axis is the reduced temperature (normalized by the instability temperature). (A) and (B) are calculated by the Krivoglaz-Clapp-Moss formula and the CVM formula, respectively.

Fig. 11 Computer simulated (100) diffraction pattern based on the BW approximation for $T=0.95/T_0$.

Fig. 12 Computer simulated (100) diffraction pattern at c=0.50 based on the CVM for $T=0.95/T_0$.

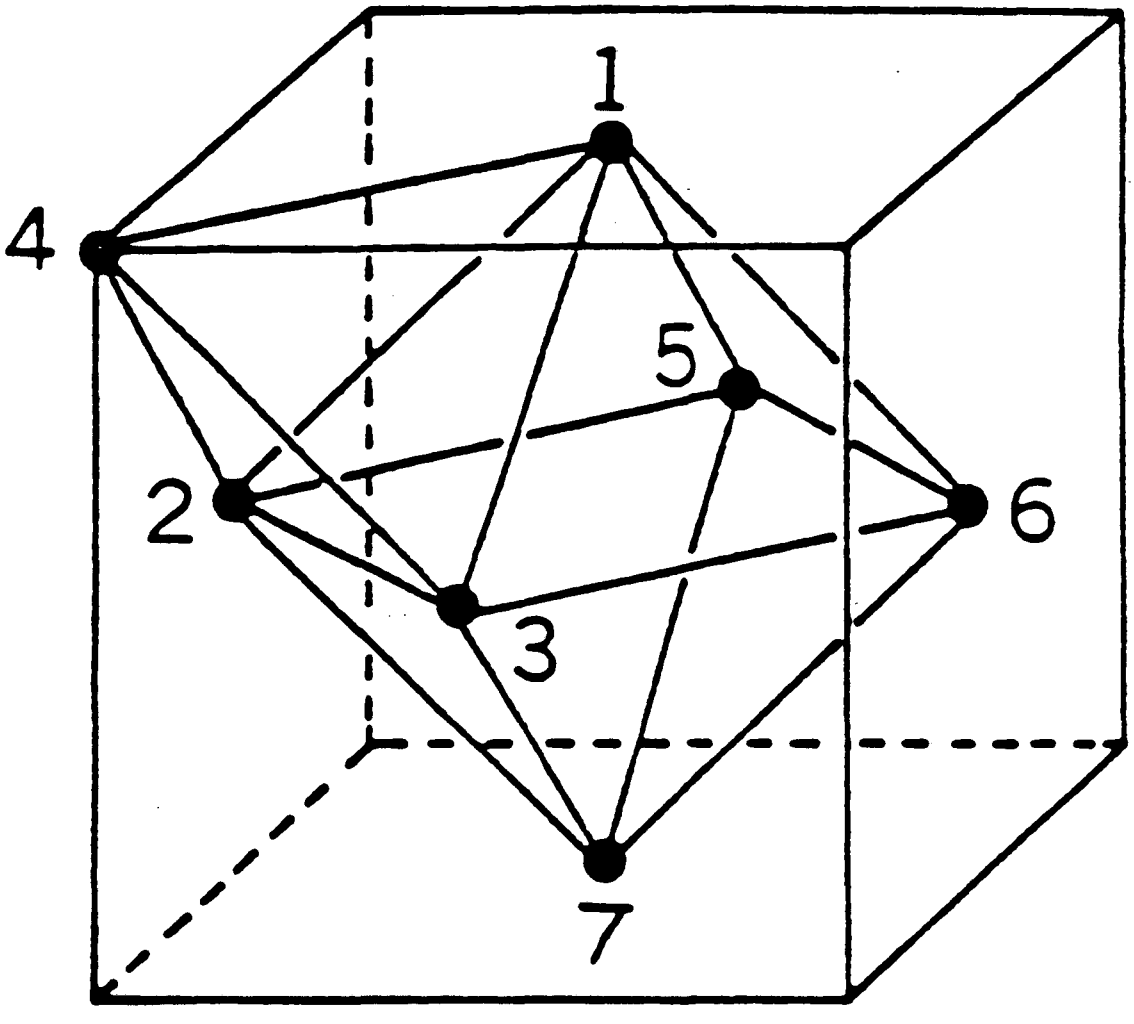

XBL 846-2313

Fig. 1

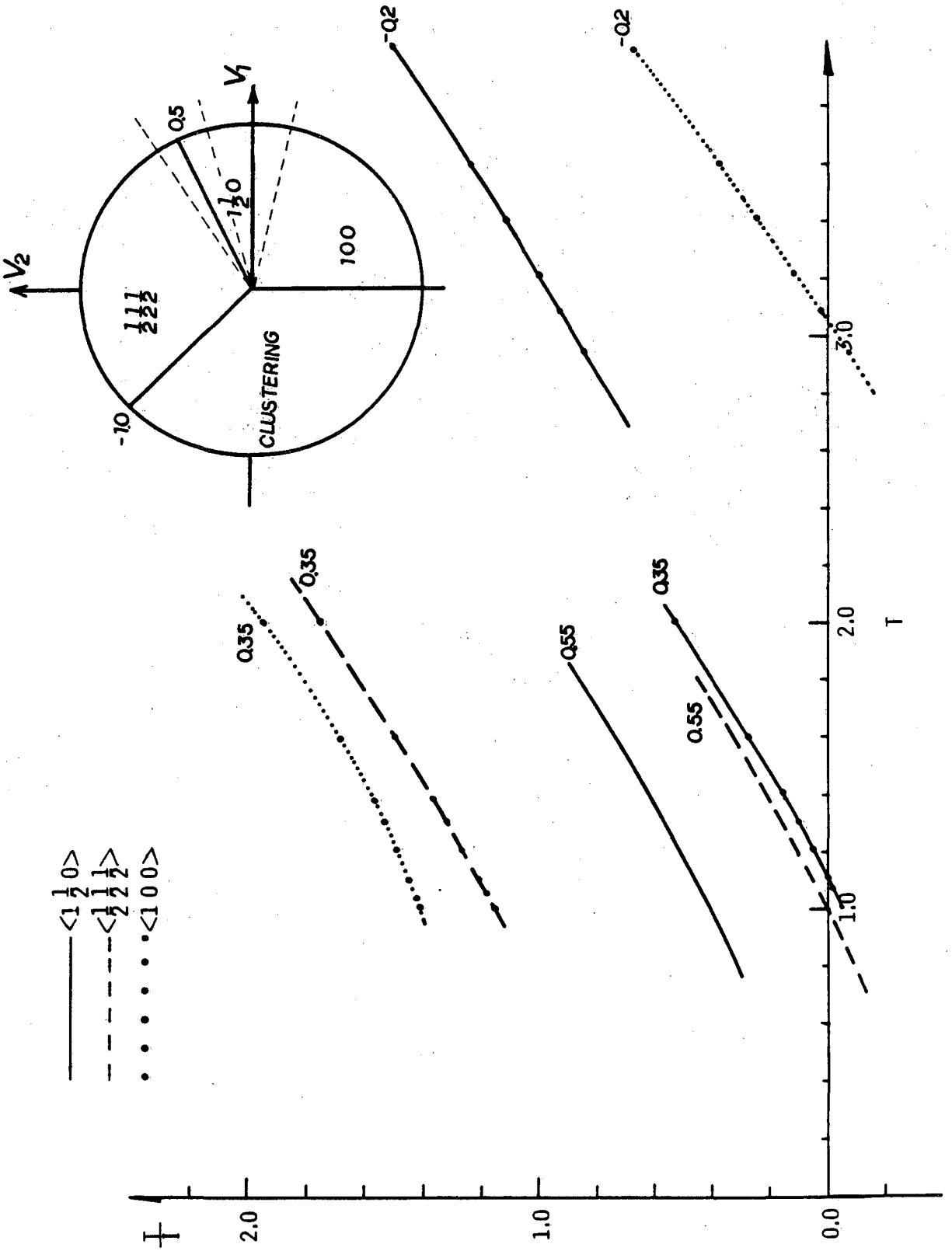

XBL 846-2574

Fig. 2

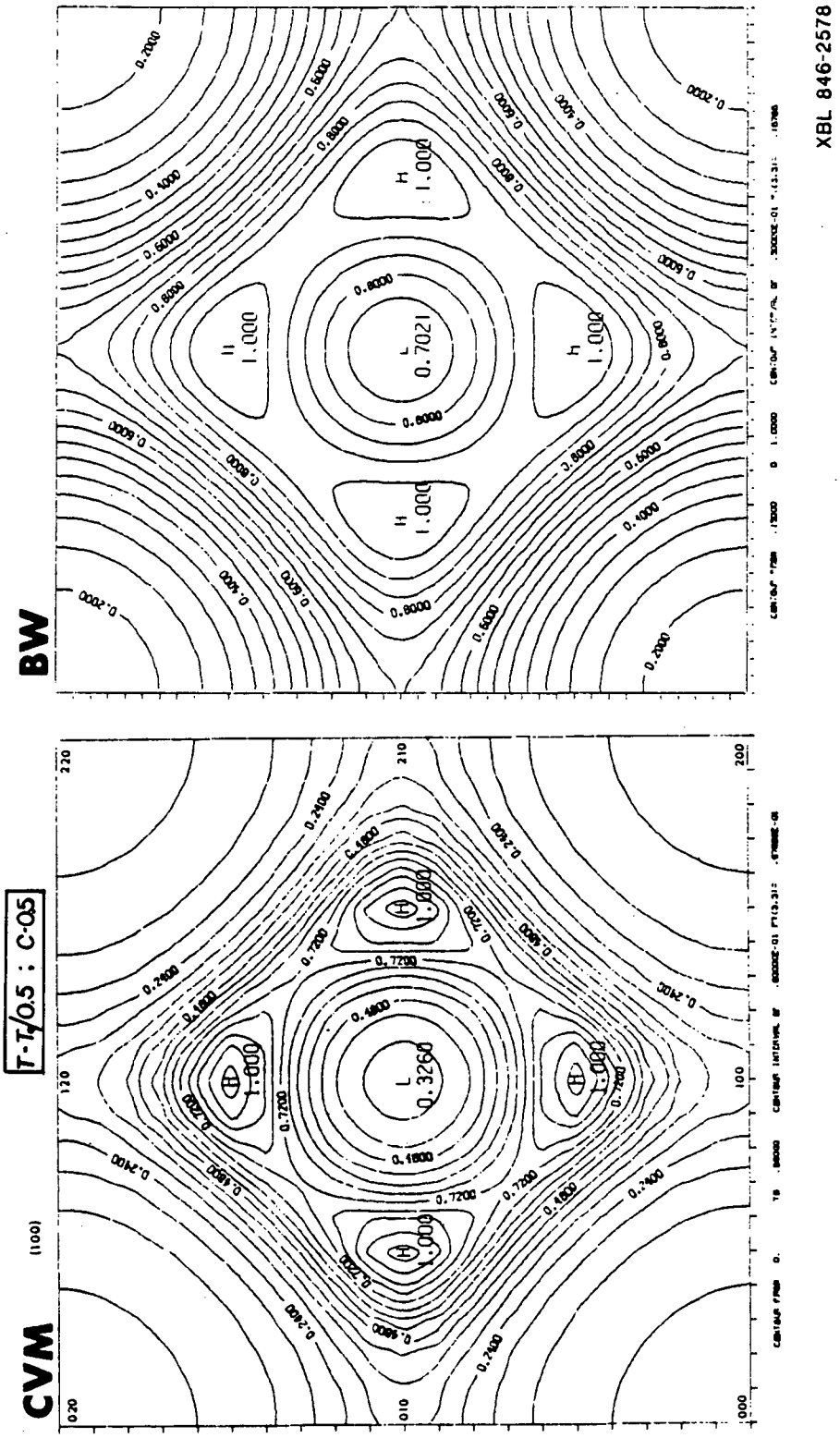
CVM
T-T_c/0.5 : C-05
(100)
020
010
000
120
110
100
220
210
200
1.000
0.3260
0.7021
0.7200
0.4800
0.2400
0.1600
BW
0.8000
0.6000
0.4000
0.2000
XBL 846-2578

Fig. 3

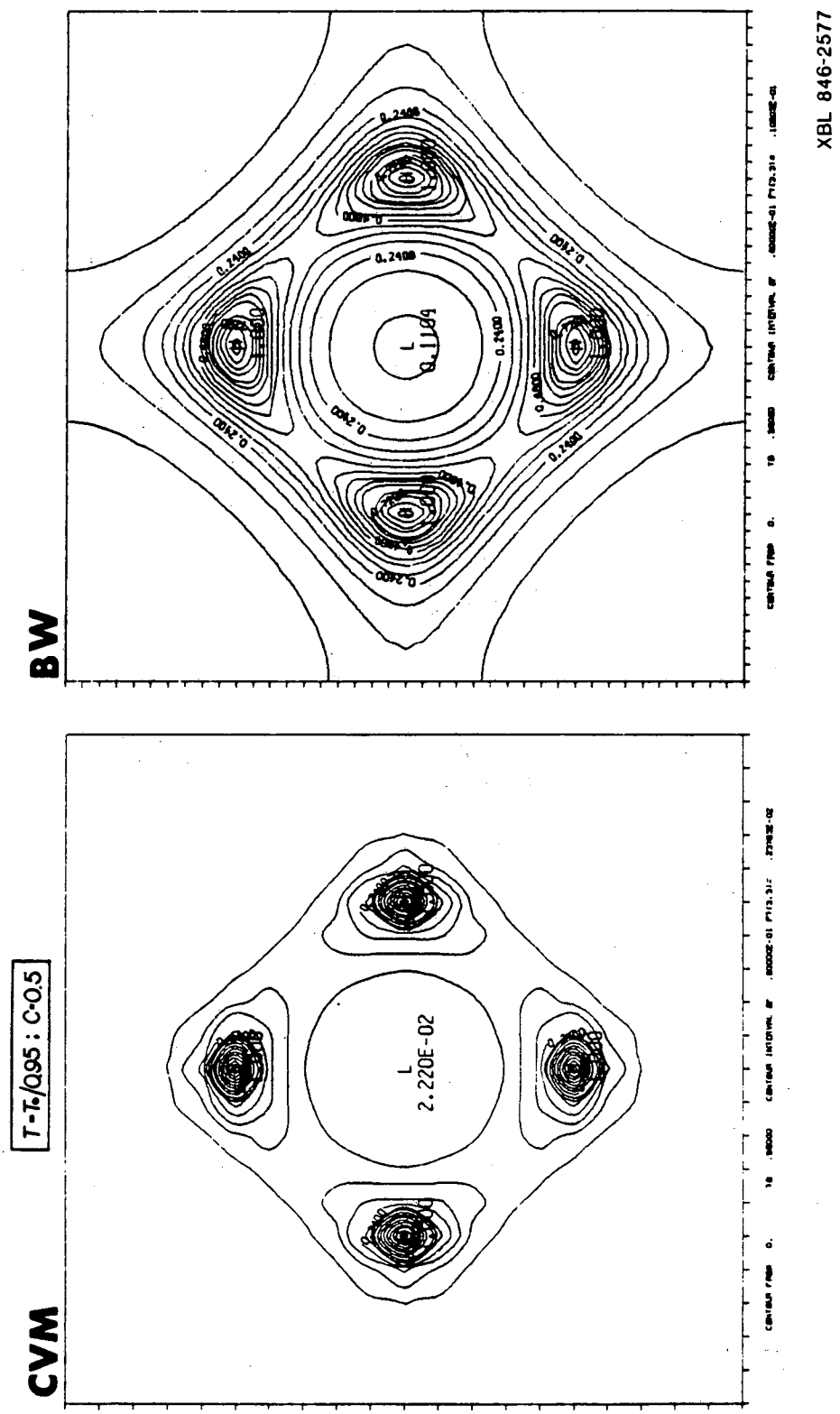

XBL 846-2577

Fig. 4

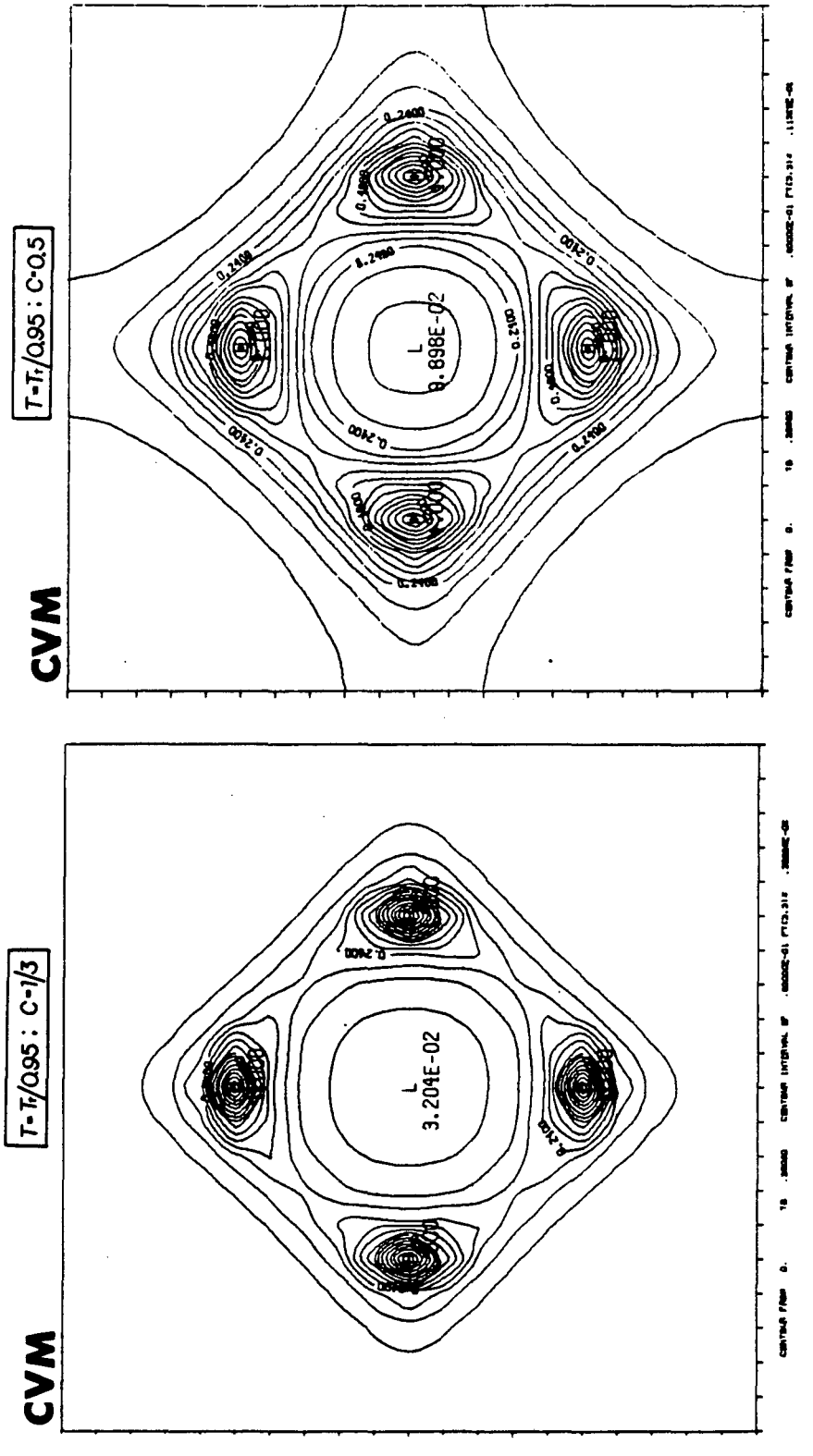

XBL 846-2579

Fig. 5

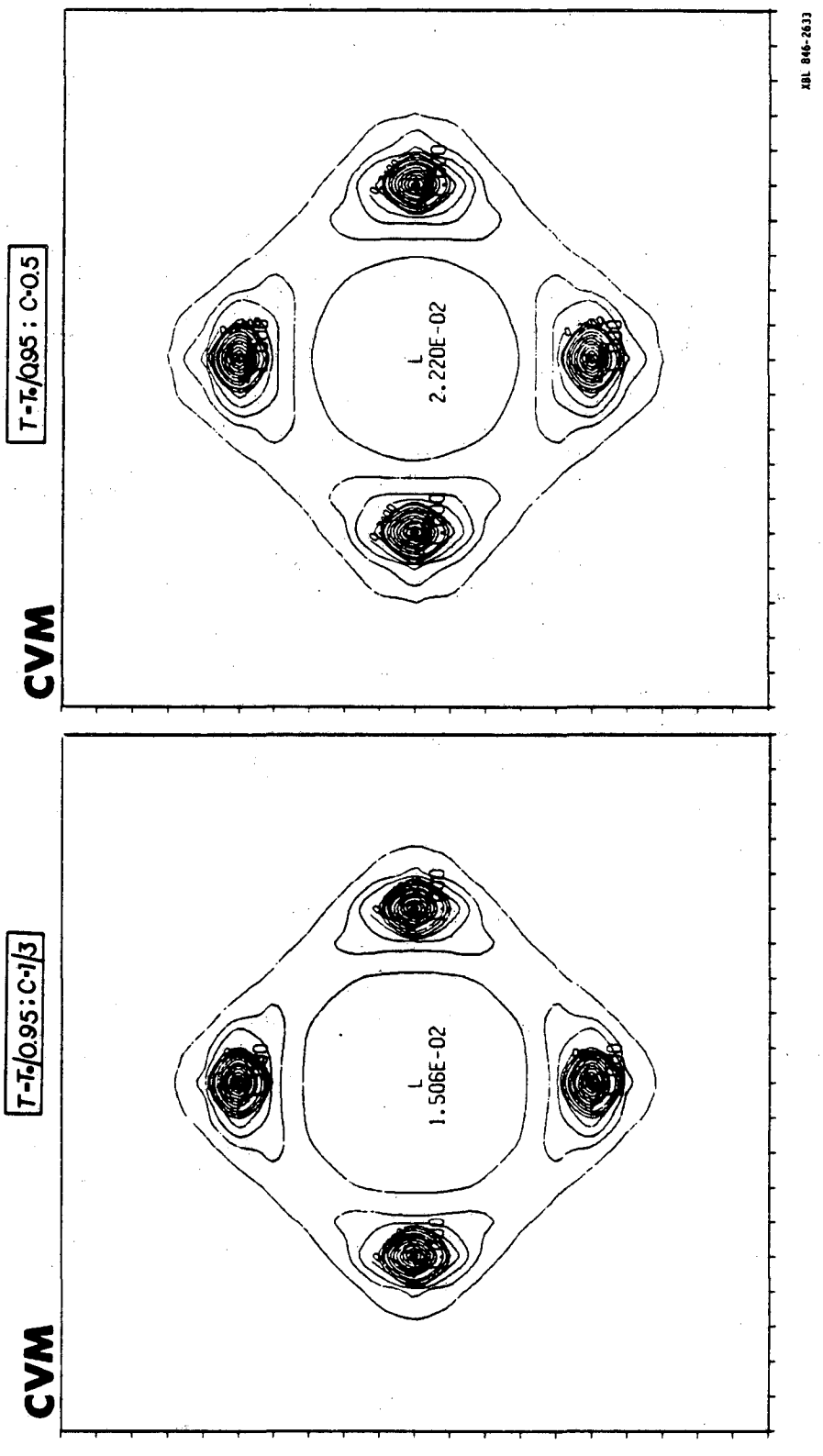

Fig. 6

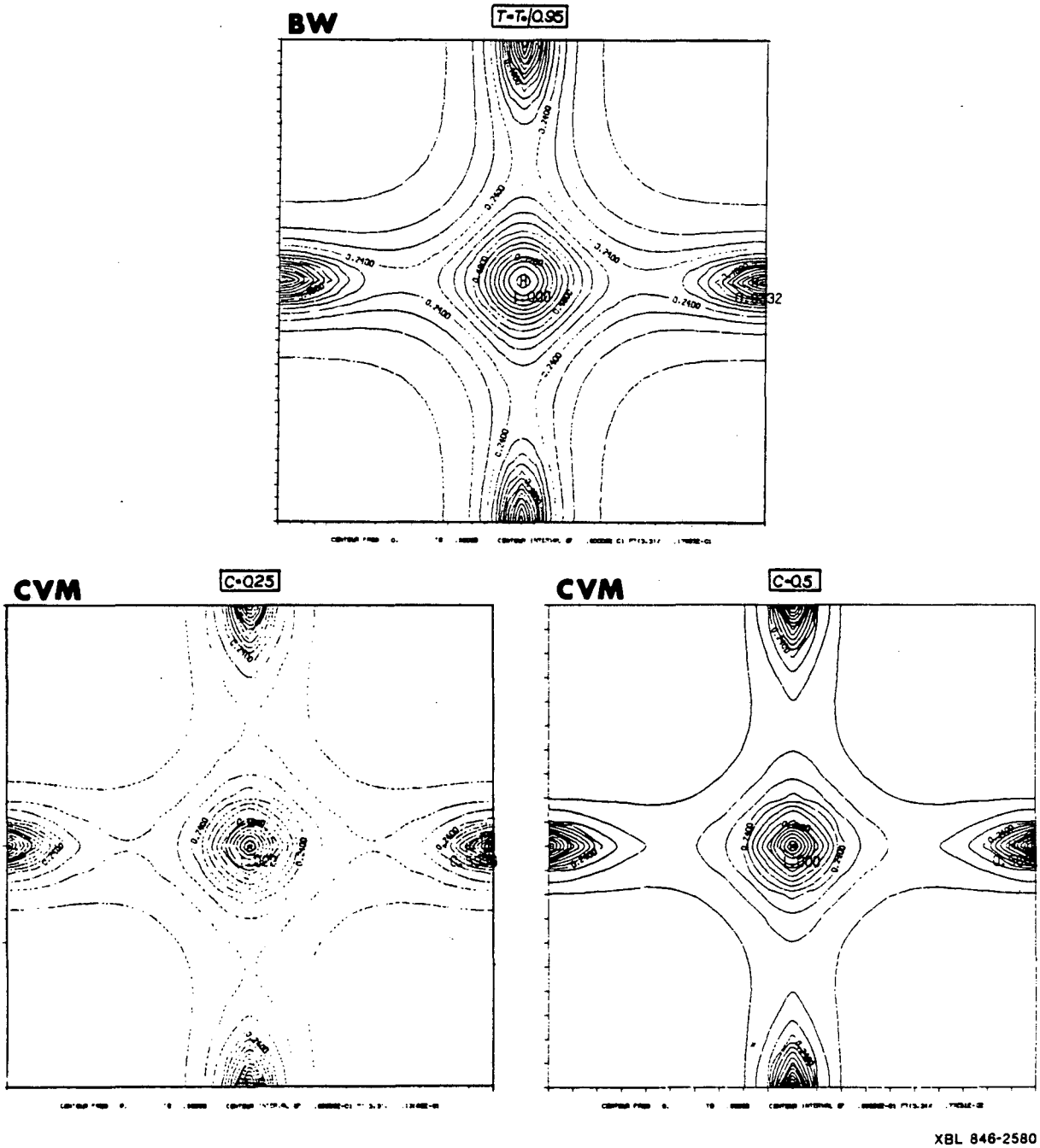

Fig. 7

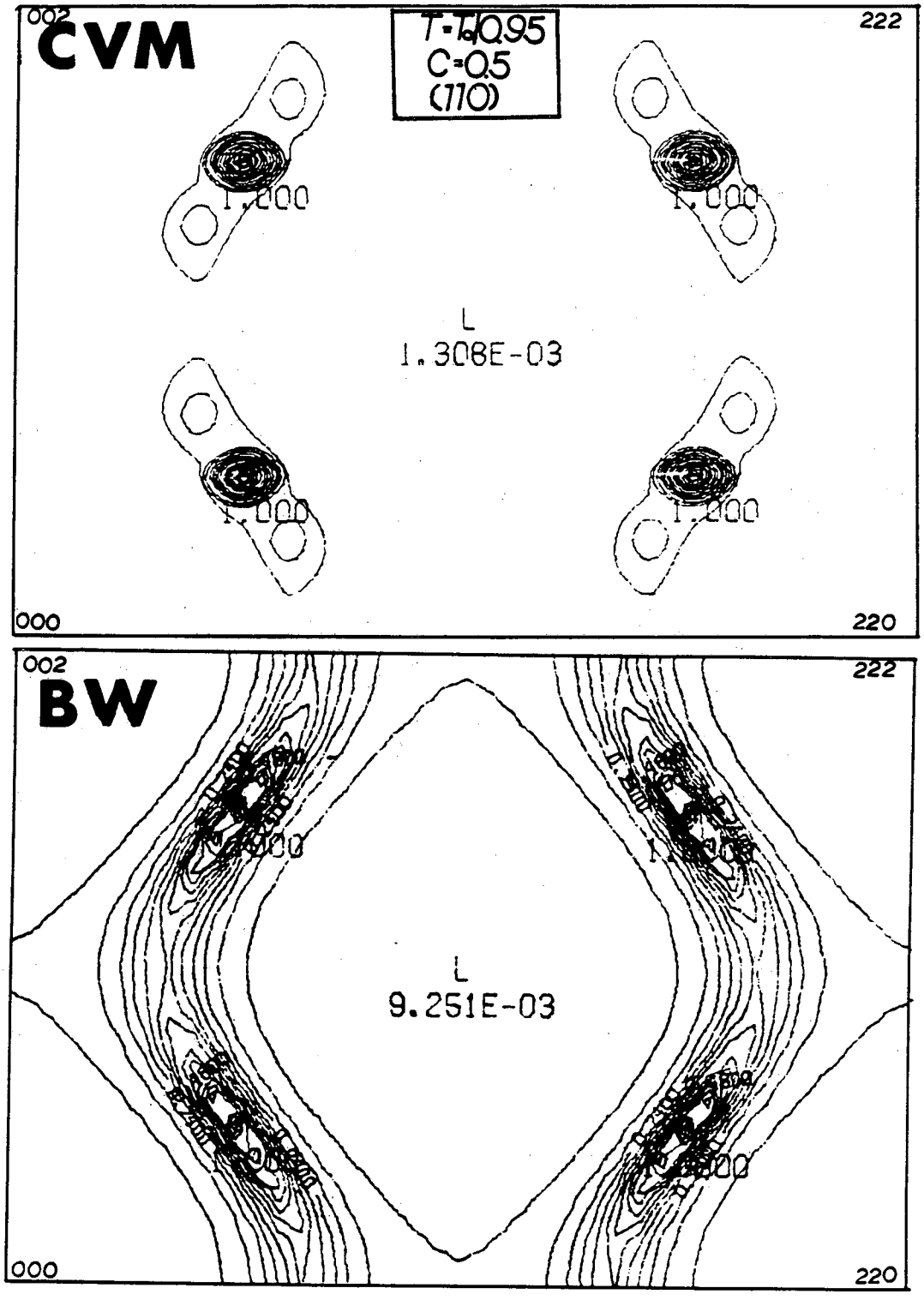

XBL 846-2573

Fig. 8

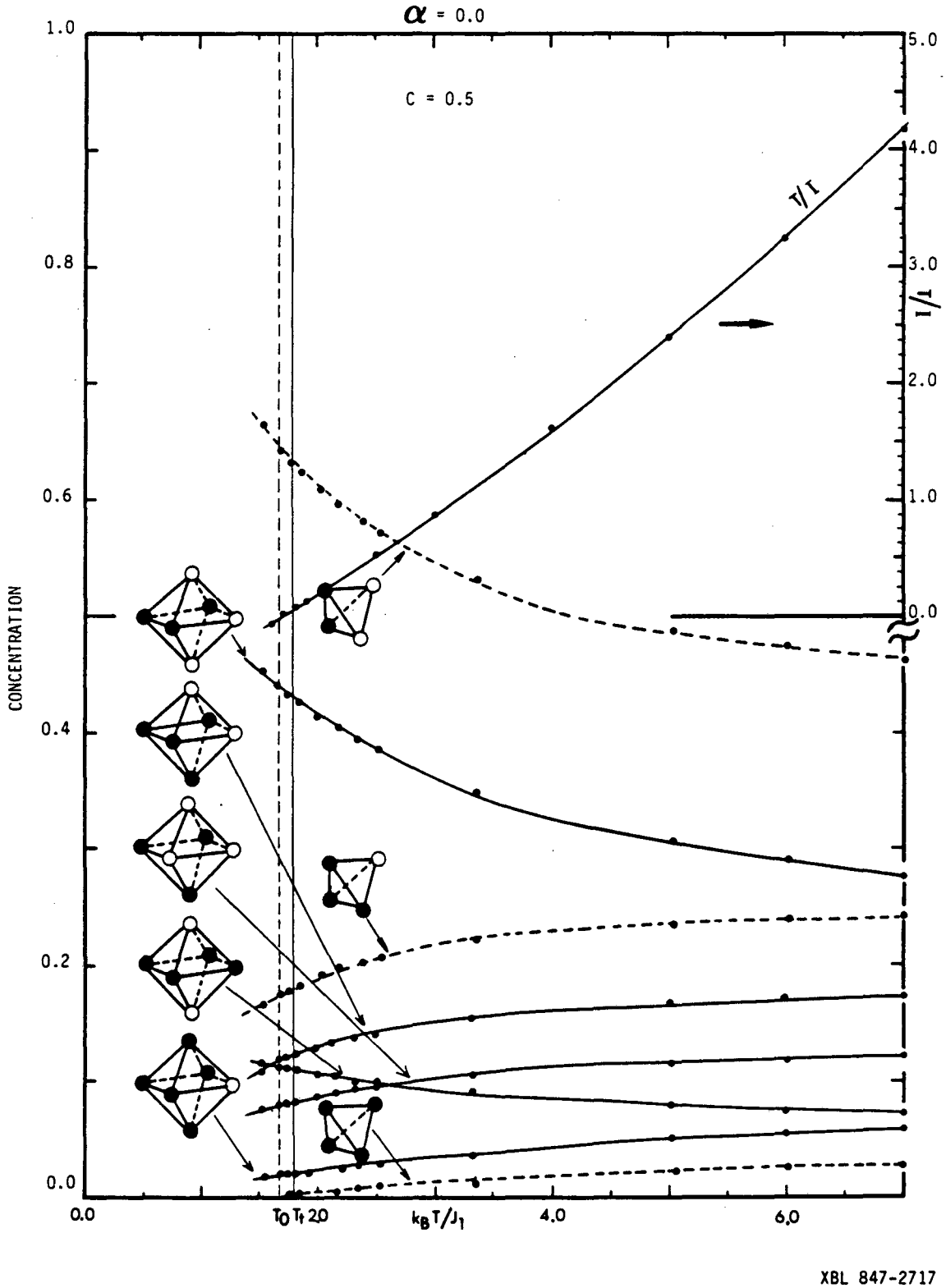

XBL 847-2717

Fig. 9

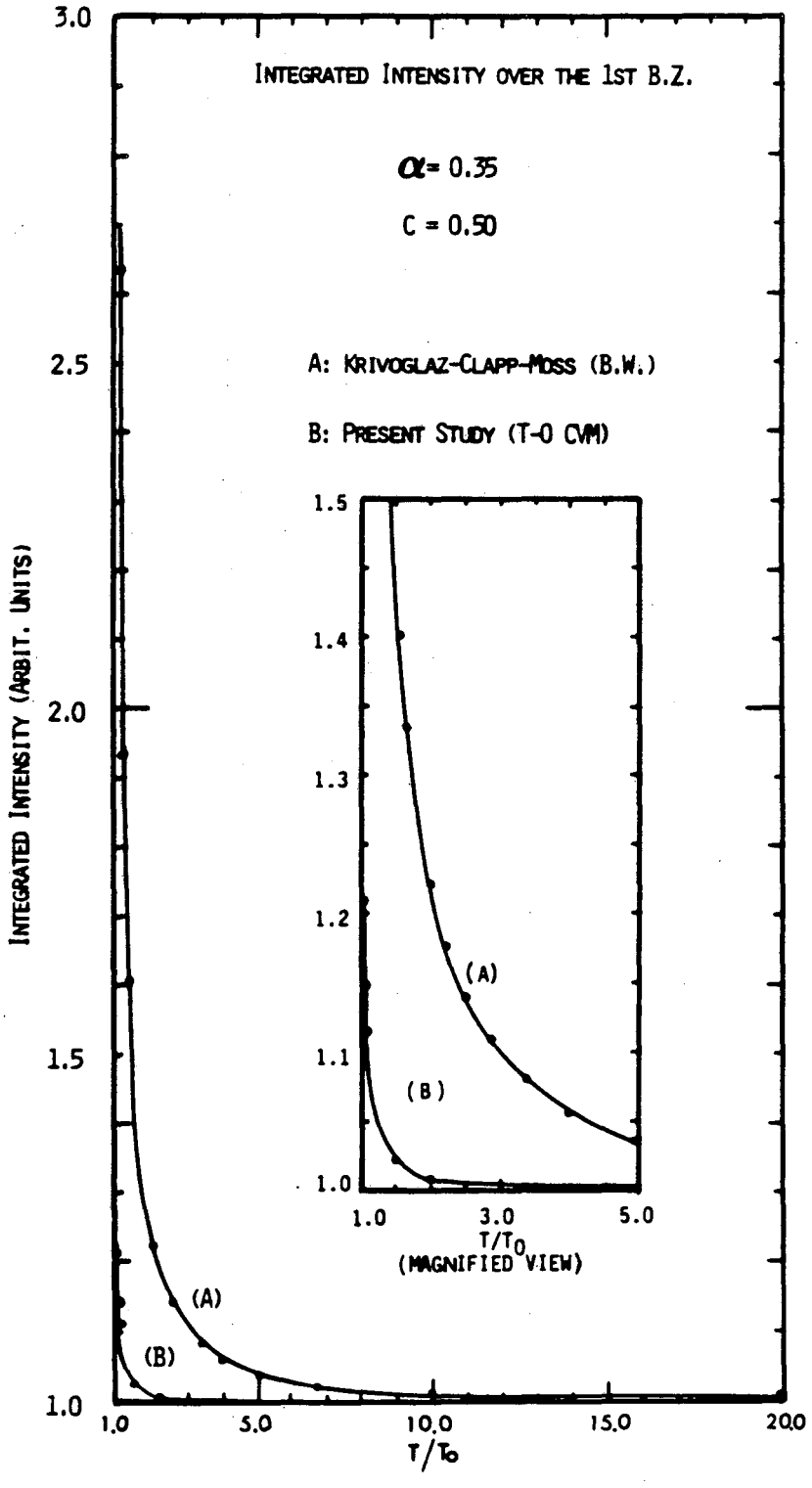
INTEGRATED INTENSITY OVER THE 1ST B.Z.
α= 0.35
C = 0.50
A: KRIVOGLAZ-CLAPP-MOSS (B.W.)
B: PRESENT STUDY (T-0 CVM)
INTEGRATED INTENSITY (ARBIT. UNITS)
3.0
2.5
2.0
1.5
1.0
1.0
5.0
10.0
15.0
20.0
T/T0
(A)
(B)
1.5
1.4
1.3
1.2
1.1
1.0
1.0
3.0
5.0
T/T0
(MAGNIFIED VIEW)
XBL 847-2660

Fig. 10

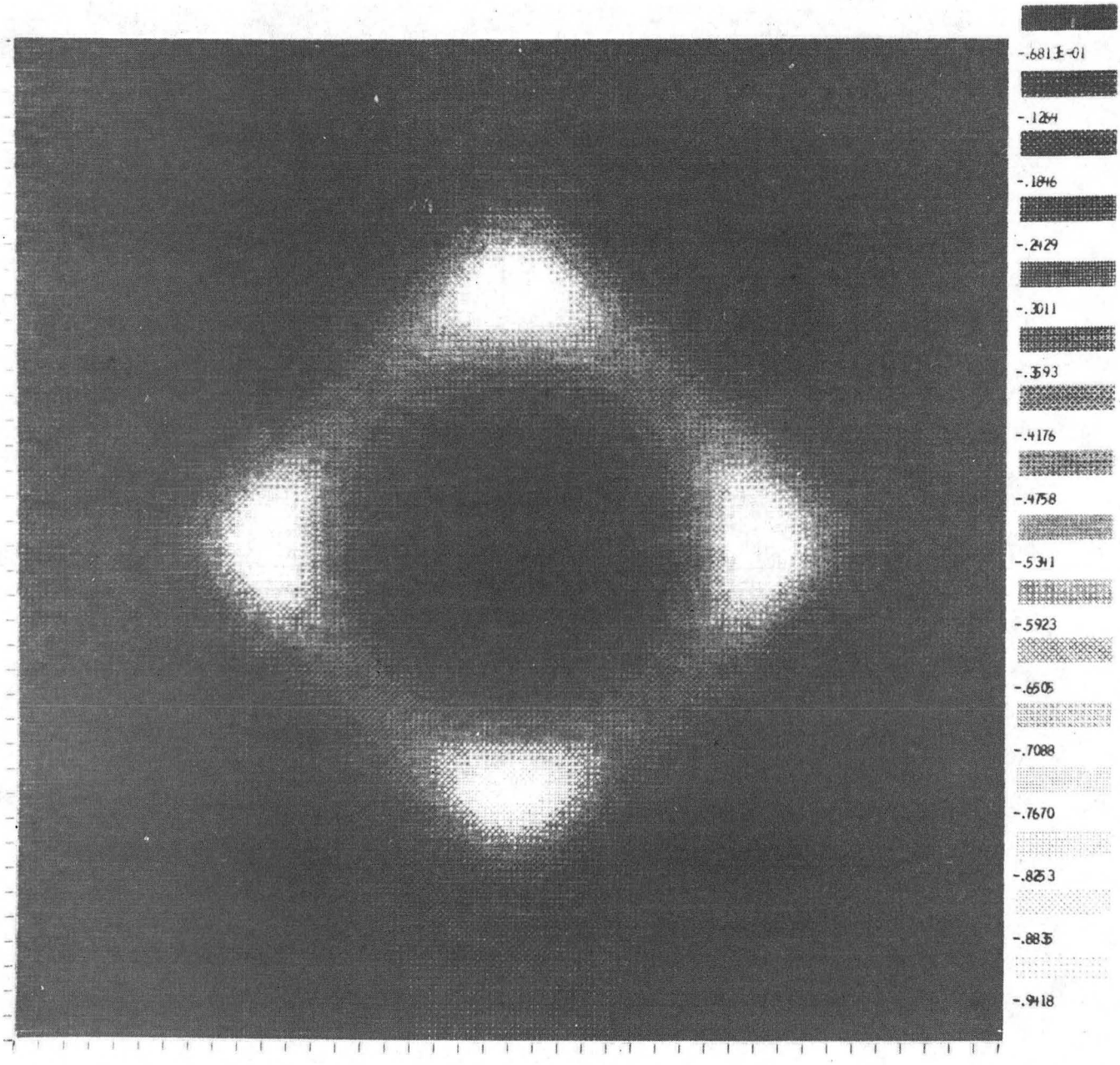

XBB 846-4728

Fig. 11

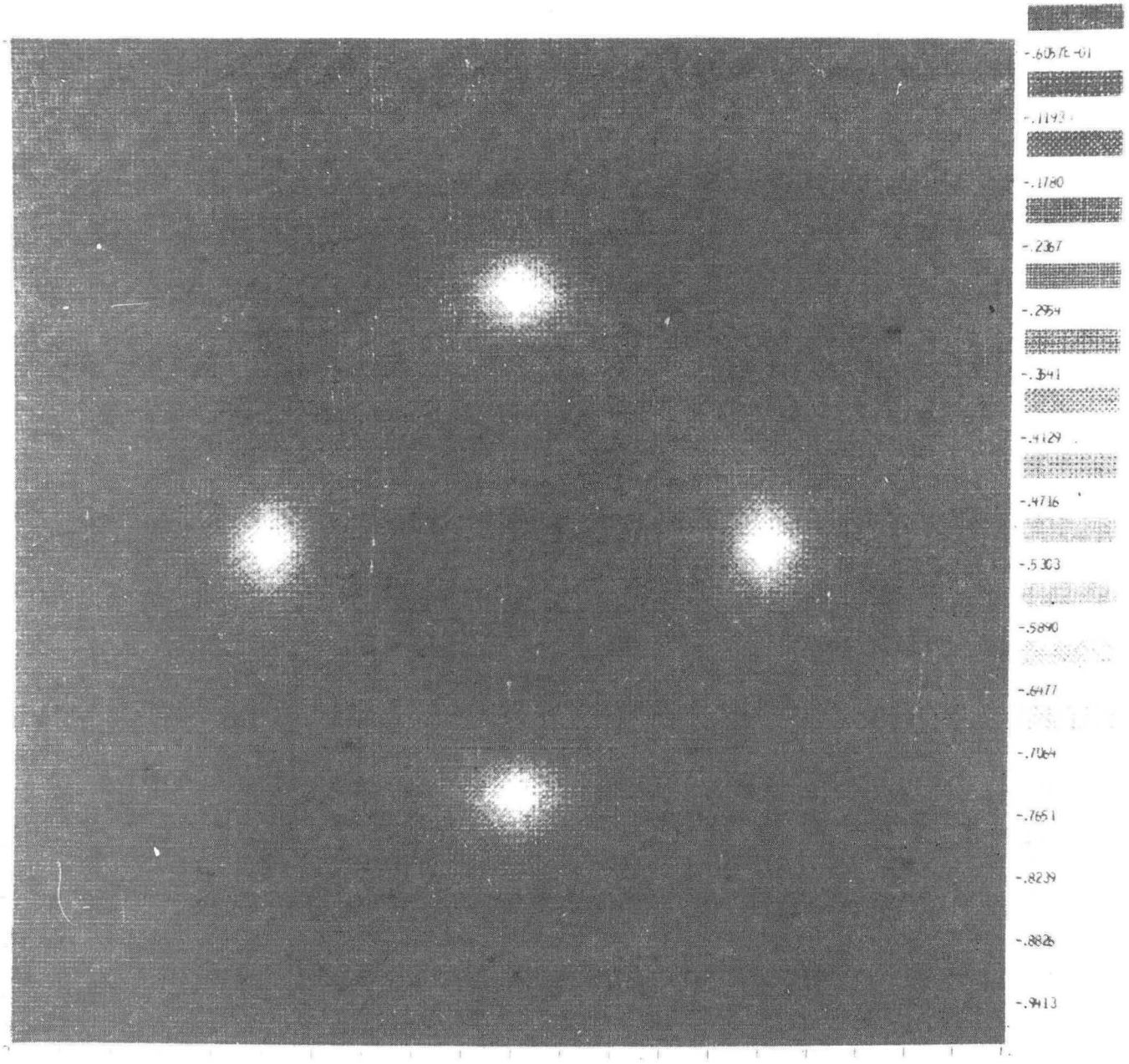

XBB 846-4729

Fig. 12

TECHNICAL INFORMATION DEPARTMENT
LAWRENCE BERKELEY LABORATORY
UNIVERSITY OF CALIFORNIA
BERKELEY, CALIFORNIA 94720